mater.scichina.com link.springer.com

Published online 2 March 2022 | https://doi.org/10.1007/s40843-021-1949-9
Sci China Mater 2022, 65(7): 1825–1832

Nanoporous nickel with rich adsorbed oxygen for efficient alkaline hydrogen evolution electrocatalysis

Qingfeng Hu[1], Zelin Chen[2*], Jiajun Wang[1,3], Xuerong Zheng[1], Xiaopeng Han[1], Yida Deng[1,2*] and Wenbin Hu[1,3]

ABSTRACT **Sluggish water dissociation kinetics severely limits the rate of alkaline electrocatalytic hydrogen evolution reaction (HER). Therefore, finding highly active electrocatalysts and clarifying the mechanism of water dissociation are challenging but important. In this study, we report an integrated nanoporous nickel (np-Ni) catalyst with high alkaline HER performance and the origin of the corresponding enhanced catalytic activity. In 1 mol L^{-1} KOH solution, this np-Ni electrode shows an HER overpotential of 20 mV at 10 mA cm^{-2}, along with fast water dissociation kinetics. The excellent performance is not only attributed to the large surface area provided by the three-dimensional interconnected conductive network but also from the enhanced intrinsic activity induced by the unique surface properties. Further studies reveal that the types of oxygen species that naturally form on the Ni surface play a key role in water dissociation. Remarkably, when the lattice oxygen almost disappears, the Ni surface terminates with adsorbed oxygen (O_{ads}), exhibiting the fastest water dissociation kinetics. Density functional theory calculation suggests that when O_{ads} acts as the surface termination of Ni metal, the orientation and configuration of polar water molecules are strongly affected by O_{ads}. Finally, the H–OH bond of interfacial water molecules is effectively activated in a manner similar to hydrogen bonding. This work not only identifies a high-performance and low-cost electrocatalyst but also provides new insights into the chemical processes underlying water dissociation, thus benefiting the rational design of electrocatalysts.**

Keywords: alkaline hydrogen evolution, water dissociation, electron redistribution, adsorbed oxygen, hydrogen bond

INTRODUCTION

Hydrogen production from electrocatalytic water splitting driven by photovoltaic or wind power systems represents an ideal, clean, and sustainable new-generation energy mode; thus, it has attracted considerable attention in recent years [1–4]. Although an alkaline environment is more suitable for electrocatalytic water splitting, the hydrogen evolution reaction (HER) kinetics is much slower in base than that in acid [5–8]. It is generally believed that the reason for the slow kinetics of alkaline HER is the lack of H^+ ions and that the formation rate of adsorption hydrogen (H_{ads}) highly depends on the water dissociation process with higher activation energy [9–12]. Thus, the Volmer step ($H_2O + e^- \rightarrow H_{ads} + OH^-$) is usually the rate determination step (RDS). Obviously, both the proton-coupled electron transfer and the dissociation of water molecules (i.e., the cleavage of the strong H–OH bond) serve as key steps in this process. During the last decade, several studies have reported the effectiveness of an important strategy, namely, the construction of metal/metal oxide species interface, which can help promote the dissociation of water molecules [13–15]. In this strategy, metal provides suitable H adsorption sites, and metal oxide assists in activating water molecules in a process called the "bifunctional mechanism" [16]. However, due to the lack of sufficient knowledge on the exact nature of catalysts, the electrochemical mechanism of water dissociation reaction has yet to be fully revealed.

Thus, to explore the HER mechanism in an alkaline environment, finding suitable catalysts with different activities and revealing the key factors leading to differences in catalytic activity are very important. Nanoscale metal catalysts often exhibit different surface nature and catalytic activities from bulk materials [17–19], which may provide a good opportunity to study the origin of the difference in alkaline HER activity. In terms of composition design, Ni-based or Ni-containing materials are a highly important class of catalysts with good catalytic activity toward HER [20–24]. High expectations have been placed on the ability of Ni to reduce dependence on precious metals and even completely replace precious metal catalysts. In terms of structural design, nanoporous metals provide a good example as they not only have the size characteristics of bulk metal on the macroscopic level but also exhibit the unique surface structure of nano-metal on the microscopic level [25–28]. In particular, their bicontinuous structural features, such as high surface area, metal conductive networks, and abundant channels, are conducive to electron conduction and mass transportation. Therefore, nanoporous metallic Ni and conventional bulk Ni materials can be used as a set of suitable comparison catalysts. This can be an appropriate opportunity to

[1] School of Materials Science and Engineering, Key Laboratory of Advanced Ceramics and Machining Technology of Ministry of Education, Tianjin University, Tianjin 300072, China
[2] State Key Laboratory of Marine Resource Utilization in South China Sea, School of Materials Science and Engineering, Hainan University, Haikou 570228, China
[3] Joint School of National University of Singapore and Tianjin University, International Campus of Tianjin University, Binhai New City, Fuzhou 350207, China
[*] Corresponding authors (emails: zelinchen@hainanu.edu.cn (Chen Z); yida.deng@tju.edu.cn or yd_deng@hainanu.edu.cn (Deng Y))

investigate the origin of the differences in activities.

In the current study, we report a nanoporous nickel (np-Ni) catalyst with high alkaline HER performance and investigate the origin of the corresponding enhanced catalytic activity. The integrated np-Ni electrode was fabricated by rapid surface dealloying of a flexible $Ni_{45}Zr_{35}Ti_{20}$ metallic glass (MG) precursor ribbon, which was directly used as the cathode to investigate the HER kinetics in 1 mol L^{-1} KOH solution. Impressively, compared with that of the bulk metal material with the corresponding alloy composition, the np-Ni electrode shows a significantly lower open circuit potential (OCP) in the actual electrolyte environment, thus indicating its unique surface electrochemical properties. Furthermore, the optimal np-Ni electrode exhibits excellent HER performance with a low overpotential of 20 mV at the geometric current density (j_{geo}) of 10 mA cm^{-2} and a small Tafel slope of 42 mV dec^{-1}, as well as the lowest OCP, which delivers faster water dissociation kinetics than that of bulk catalysts. X-ray and ultraviolet photoelectron spectroscopy (XPS and UPS, respectively) results reveal that the np-Ni tends to form a nickel/adsorbed oxygen (Ni-O_{ads}) surface structure. Further, the differential charge density results confirm that electron transfer from the metal surface to O_{ads} is allowed, which induces the electron redistribution on the np-Ni surface and causes the change of surface properties. The Ni-O_{ads} model can be well used to explain the experimental observations. Finally, combined with the theoretical calculation results, we discuss the role of O_{ads} in promoting the Volmer step.

RESULTS AND DISCUSSION

The fabrication procedure of the integrated MG/np-Ni electrode is illustrated in Fig. 1a. The $Ni_{45}Zr_{35}Ti_{20}$ (at%) MG ribbons (see Fig. S1a) prepared by single-roller melt spinning were used as the precursors to fabricate integrated np-Ni electrodes by the dealloying method. Under the corrosive condition of hydrofluoric acid, the more active Zr and Ti on the precursor surface were selectively removed in large quantities, while the remaining inert Ni atoms formed the porous structure skin covering the MG matrix, resulting in an integrated np-Ni electrode (see Fig. S1b). The np-Ni electrode was directly used as the electrocatalysts for HER in an alkaline solution (see Video S1). Its geometry is examined in detail by scanning electron microscopy (SEM, Fig. S2). The np-Ni electrode with good mechanical connectivity shows an obvious open foam-liked structure. Rich, small pores and continuous ligaments can be observed in the

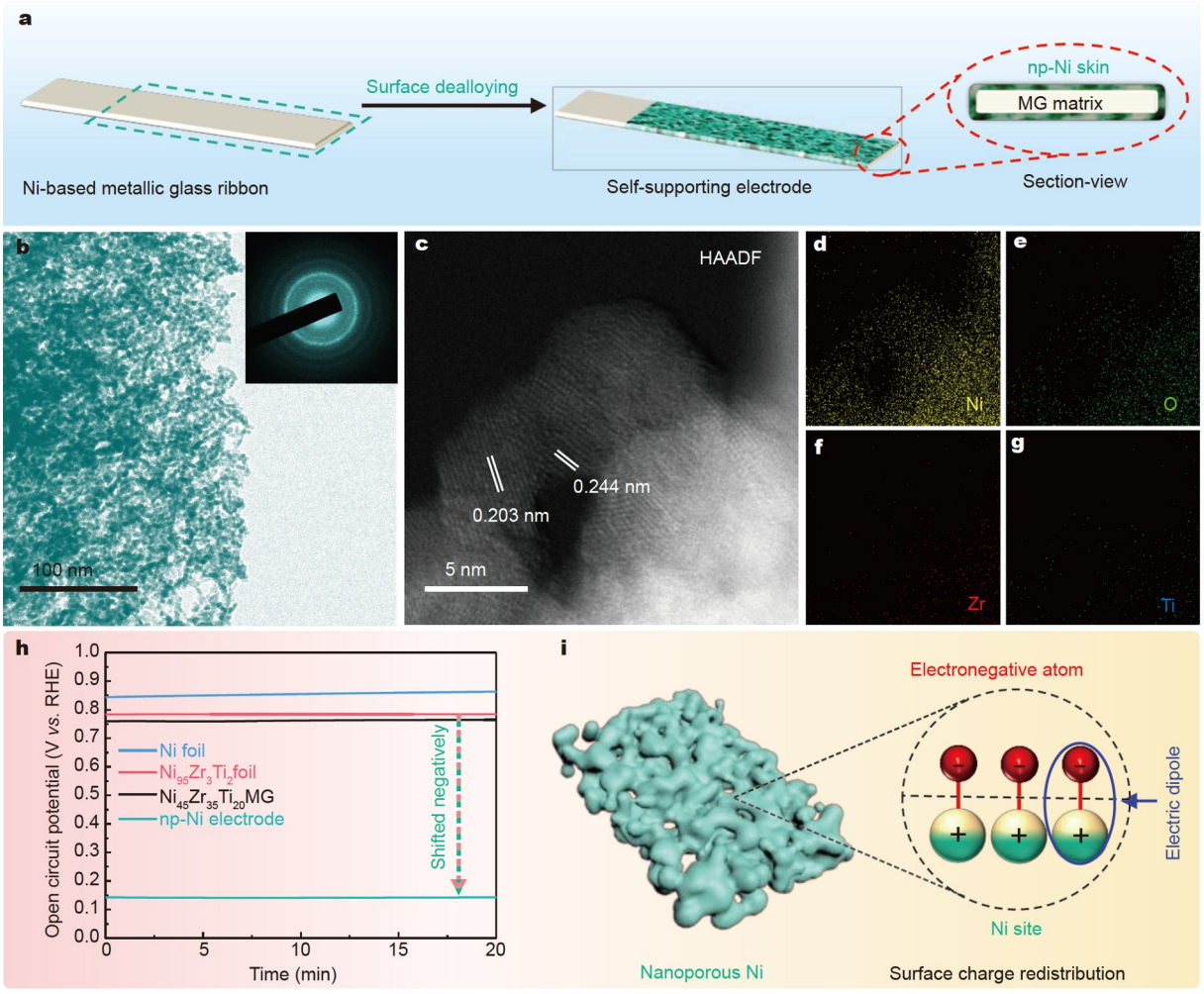

Figure 1 Preparation and characterization of the np-Ni electrode. (a) Schematic illustration of the integrated np-Ni electrode fabrication. (b) TEM image of np-Ni. Inset: SAED pattern of np-Ni. (c) HAADF-STEM image of np-Ni and (d–g) the corresponding elemental mappings of Ni, O, Zr, and Ti, respectively. (h) OCP of various samples in 1 mol L^{-1} KOH, with a Hg/HgO electrode as the reference electrode. (i) Schematic illustration of the surface charge distribution characteristics of np-Ni.

images generated through transmission electron microscopy (TEM) (Fig. 1b) and high-angle annular dark-field scanning TEM (HAADF-STEM) (Fig. S3). Such a structure facilitates mass transport and increases the catalyst surface area. Furthermore, the selected area electron diffraction (SAED) image of np-Ni displays a typical ring-like diffraction pattern (Fig. 1b, inset), indicating its polycrystalline structure. Energy-dispersive X-ray spectroscopy (EDS) analysis (Fig. S4) reveals the composition of the optimal np-Ni, that is, $Ni_{95}Zr_3Ti_2$. Therefore, in the subsequent research, the $Ni_{95}Zr_3Ti_2$ alloy foil was introduced as a bulk reference catalyst. Due to the threshold effect in the dealloying method, it was difficult to remove the residual Zr and Ti elements in the nanoporous ligament. The HAADF-STEM image (Fig. 1c) shows that the ligament is composed of nanoscale grains accompanied by an undulating surface profile. The lattice distances of 0.203 and 0.244 nm are assigned to the metallic Ni (111) plane (PDF#04-0850) and the NiO (111) plane (PDF#47-1049), respectively. The corresponding EDS element mappings (Fig. 1d–g) indicate the uniform distribution of residual elements in the ligament of np-Ni. In addition, the signal of oxygen was also observed, indicating that the real surface of the sample is not an ideal metal surface.

The crystalline structures of np-Ni were analyzed by X-ray diffraction (XRD, Fig. S5). Pure Ni foil, $Ni_{95}Zr_3Ti_2$ alloy foil, and $Ni_{45}Zr_{35}Ti_{20}$ MG ribbon samples were used for comparison. The sharp XRD peaks of Ni foil and $Ni_{95}Zr_3Ti_2$ alloy foil at 44.5° correspond to the face-centered cubic (fcc)-Ni (111) plane, demonstrating good crystallinity. In comparison, the $Ni_{45}Zr_{35}Ti_{20}$ MG ribbons exhibit a dispersive diffraction peak, demonstrating their amorphous structure. After dealloying the $Ni_{45}Zr_{35}Ti_{20}$ MG ribbons, a new broadened diffraction peak appeared around 44.5°, indicating the presence of local structural disorder in the prepared np-Ni [29]. The introduction of rich grain boundaries in the nanomaterials with polycrystalline structure results in structural disorder due to local crystal cell volume expansion/contraction [30]. Further, high-resolution TEM (HRTEM) images (Fig. S6) exhibit the poor crystallinity of the np-Ni, because continuous and regular lattice fringes are difficult to observe in a large range. Nevertheless, this result is in accordance with the dispersion characteristics of the electron diffraction ring (Fig. 1b, inset) and the broadening characteristics of the XRD peaks in Fig. S5.

Before conducting further testing, we first investigated the OCP of various electrodes in the actual electrolytic cell environment (based on the same reference electrode). OCP is used to indicate the difference in surface potential. As shown in Fig. 1h, the OCP values of pure Ni foil, $Ni_{95}Zr_3Ti_2$ foil, and $Ni_{45}Zr_{35}Ti_{20}$ MG electrodes are all around 0.8 V_{RHE} (V *vs.* reversible hydrogen electrode (RHE)). In comparison, the OCP of the np-Ni electrode is ~0.14 V_{RHE}, which is significantly lower than those of other samples. Taking into account the condition of electrical neutrality, the shift of surface potential is related to the change of surface charge distribution caused by dipoles [31–33]. This means that the presence of appropriate atoms with greater electronegativity generates electric dipoles on the np-Ni surface. In turn, this results in the change in local surface polarity, which produces a phenomenon similar to the effect of injecting negative charges, as illustrated in Fig. 1i.

Next, we investigated the HER kinetics of these samples in a 1 mol L^{-1} KOH solution. In linear sweep voltammetry (LSV) plots (Fig. 2a), $Ni_{45}Zr_{35}Ti_{20}$ MG shows the worst HER performance, and its overpotential is as high as ~500 mV at the j_{geo} of 10 mA cm^{-2}, followed by those of $Ni_{95}Zr_3Ti_2$ alloy foil (265 mV) and Ni foil (255 mV). Markedly, the np-Ni shows an ultralow overpotential of 20 mV at the j_{geo} of 10 mA cm^{-2}, which is among the best performances of the noble metal-free electrocatalysts (see Table S1). Further, the kinetics information of HER can be identified by the corresponding Tafel analysis

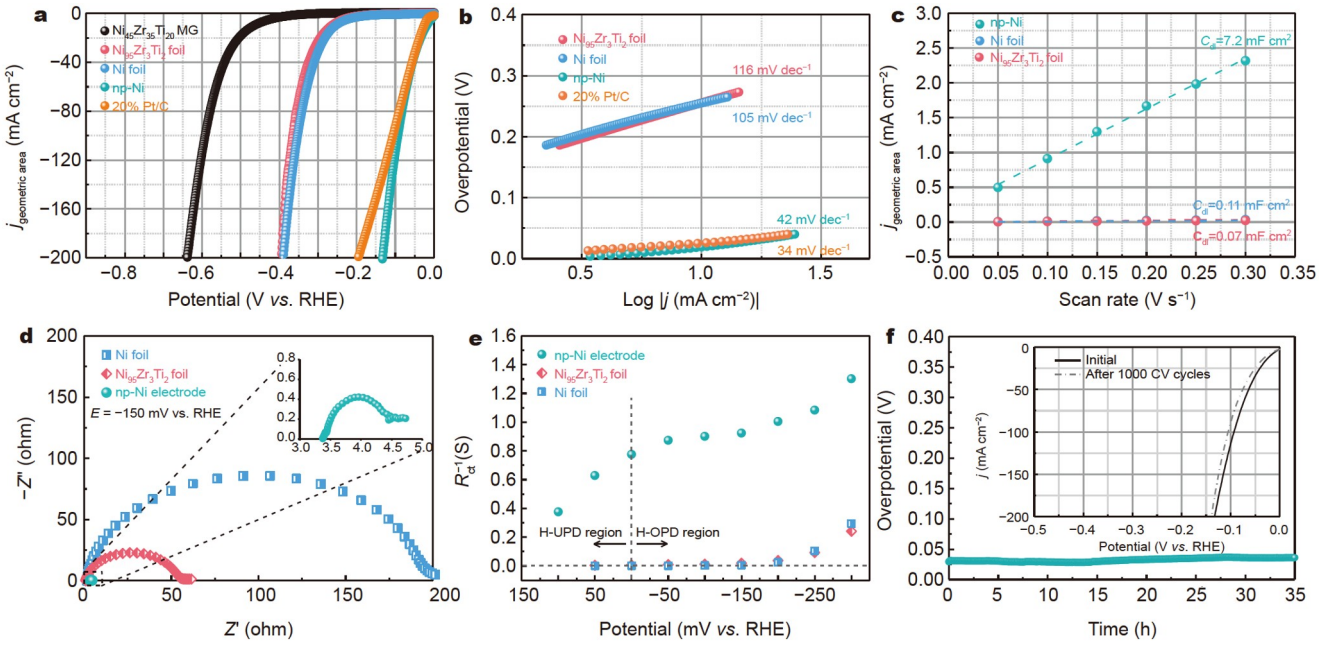

Figure 2 The electrochemical results of various catalysts in 1 mol L^{-1} KOH solution. (a) LSV plots measured at 1 mV s^{-1}. 20% Pt/C was loaded on the carbon cloth with a loading amount of 1 mg cm^{-2}. (b) Tafel slopes. (c) C_{dl} values obtained from the CV test. (d) Nyquist plots obtained at the potential of −150 mV_{RHE}. (e) The reciprocal of the charge transfer resistance as a function of the potential value. (f) The stability test of np-Ni at constant 10 mA cm^{-2}. Inset: LSV plots of np-Ni before and after 1000 CV cycles. LSV: scan at 1 mV s^{-1}, CV: scan at 20 mV s^{-1}.

[9,10,34,35]. In Tafel plots (Fig. 2b), the Tafel slopes of Ni and $Ni_{95}Zr_3Ti_2$ alloy are 105 and 116 mV dec^{-1}, respectively, both of which are close to 120 mV dec^{-1}, indicating that the Volmer step is the RDS. In comparison, the Tafel slope of np-Ni is down to 42 mV dec^{-1}, which is close to 40 mV dec^{-1}, suggesting that the Heyrovsky step ($H_{ads} + H_2O + e^- \rightarrow H_2 + OH^-$) is the RDS.

To better understand the origin of the high catalytic efficiency of the np-Ni electrode, the contribution of the specific surface area factor was also discussed. The electrochemical surface areas (ECSA) of these electrodes were estimated by extracting the double-layer capacitance (C_{dl}) (Fig. 2c) through cyclic voltammetry (CV) measurements (see Fig. S7). The results show that, indeed, the C_{dl} of np-Ni (7.2 mF cm^{-2}) is much higher than that of Ni foil (0.11 mF cm^{-2}) and $Ni_{95}Zr_3Ti_2$ foil (0.07 mF cm^{-2}), indicating that np-Ni can provide more surface area. Subsequently, to exclude the effect of enhanced surface area, the LSV curves were normalized by ECSA instead of the geometric surface area. As shown in Fig. S8, np-Ni still exhibits the highest electrocatalytic activity among all the electrodes. This indicates that the np-Ni catalyst has good intrinsic activity. The above results suggest that the extraordinary HER activity of np-Ni is due to not only the enhanced ECSA but also the better intrinsic activity of the np-Ni catalyst. Combined with the previous analysis on RDS, it can be determined that the np-Ni catalyst mainly changes the HER kinetics by accelerating the Volmer step.

The enhanced HER performance was also verified by electrochemical impedance spectroscopy. Fig. 2d exhibits the Nyquist plots of Ni foil, $Ni_{95}Zr_3Ti_2$ alloy foil, and np-Ni electrode at the potential of −150 mV_{RHE} (mV *vs.* RHE). np-Ni holds the smallest semicircle diameter, indicating the best charge transfer behavior. More Nyquist plots of these catalysts at various potentials are shown in Fig. S9. The corresponding charge transfer resistance (R_{ct}) values are obtained from the fitting parameters for the Nyquist plots, and the results are summarized in Fig. 2e. To reflect the charge transfer behavior more intuitively, the R_{ct}^{-1} value is used as a *y* variable, where a larger R_{ct}^{-1} value represents a faster charge transfer rate. As can be clearly seen from Fig. 2e, the R_{ct}^{-1} value of np-Ni is very large both within the hydrogen underpotential deposition (H-UPD) and hydrogen overpotential deposition (H-OPD) regions, indicating the good charge transferability in the overall HER process. However, the R_{ct}^{-1} value of pure Ni and $Ni_{95}Zr_3Ti_2$ alloy electrodes is almost zero within an overpotential of less than ~200 mV. This finding indicates that in a small overpotential range, both bulk catalysts exhibit inert behavior for HER. To achieve the transition from the inert state to the active state, a greater overpotential must be applied. Obviously, this feature of bulk catalysts is unfavorable to HER.

The long-term durability of the catalyst is also an important indication for evaluating the application potential. Therefore, the stability of np-Ni was tested based on the potential *versus* time plot at constant 10 mA cm^{-2}. The results show that the np-Ni electrode has good apparent catalytic stability under the continuous hydrogen evolution mode for at least 35 h (Fig. 2f). The inset in Fig. 2f shows the LSV curves of the np-Ni electrode before and after 1000 CV cycles. The results demonstrate the excellent stability of the np-Ni electrode under the unsteady operation mode. Although the ligaments of np-Ni show a trend of coarsening to some extent after the HER stability test, rich nanopores can still be observed (Fig. S10).

The surface chemical environments and electronic structures of these catalysts were studied by spectroscopy methods combined with density functional theory (DFT) calculation. This was done to clarify the origin of the difference in surface properties between np-Ni and bulk Ni catalysts. Fig. 3a displays the XPS results of the Ni $2p_{3/2}$ spectra. For $Ni_{95}Zr_3Ti_2$ alloy and pure nickel, the characteristic peaks around 852.6 eV correspond to metallic Ni^0, and no obvious characteristic peaks corresponding to Ni in the oxidation state are observed. However, for the np-Ni electrode, the obvious characteristic peak around 855.7 eV corresponds to Ni in the oxidation state, and the characteristic peaks for metallic Ni^0 shift positively to 853.1 eV. The result indicates that the chemical properties of the np-Ni surface are more active and can easily lose electrons compared with others. Further, the surface band structures of the np-Ni electrode, $Ni_{95}Zr_3Ti_2$ alloy foil, and pure Ni foil were characterized by UPS (Fig. 3b). There are obvious differences in the shape of UPS curves between np-Ni and the bulk catalysts. At a binding energy between 4 and 8 eV (which are representative for O 2p in oxide as well as for adsorbed oxygen) [36], the relative signal intensity from the np-Ni sample shows an obvious increase. This result indicates that the np-Ni sample interacts with oxygen more easily.

The XPS signal of the oxygen species was analyzed in detail. Fig. 3c shows the surface Ni/O molar ratio based on the XPS results. As can be seen, the pure Ni surface contains a small amount of oxygen element (~13%). More oxygen element (~50%) exists on the surface of $Ni_{95}Zr_3Ti_2$ alloy, which involves the induction of doped oxygen-philic Ti and Zr elements. However, the oxygen content on the surface of the np-Ni sample is as high as ~70%, which explains why the uniformly distributed O signal is observed in EDS mapping (Fig. 1e). In the O 1s spectrum (Fig. 3d), the XPS peaks around 530.0, 531.5, and 533.0 eV, which correspond to lattice oxygen (O_L), adsorbed oxygen (O_{ads}), and oxygen-containing groups (such as adsorbed H_2O molecules), respectively [37–40]. As summarized in Fig. 3e, the signal intensity of O_{ads} is much higher than that of O_L, indicating that the true surface of np-Ni is covered with a large amount of O_{ads}, rather than an ideal metallic nickel surface. Notably, a considerable part of the O 1s signal can be derived from air pollutants, as no obvious signal corresponding to oxidation state is observed in the Ni 2p spectrum of bulk samples. In comparison, for the np-Ni sample, a significant signal corresponding to the oxidation state is observed. Therefore, it is difficult to ignore the bonding between Ni and O on the np-Ni surface.

Next, we constructed a Ni metal surface model containing adsorbed oxygen (denoted as Ni-O_{ads} model, see Fig. S11) to simulate the structure characteristics of the np-Ni surface, which is then used to explain how water molecules are activated. The differential charge density analysis (Fig. 3f) shows that O_{ads} atom can significantly affect the charge redistribution on the Ni surface, which is consistent with the observation of the Ni 2p spectrum. Therefore, the change of surface polarity induced by O_{ads} is an important reason for the negative shift of OCP. In addition, in the investigation of np-Ni samples with different surface O_L and O_{ads} ratios, changes in OCP and catalytic activity also reflect their relevance to the surface structure characteristics involving Ni/O atoms (Fig. S12, see more data and discussion in Supplementary information). In particular, the np-Ni sample, whose surface characteristics are more in line with the Ni-O_{ads}

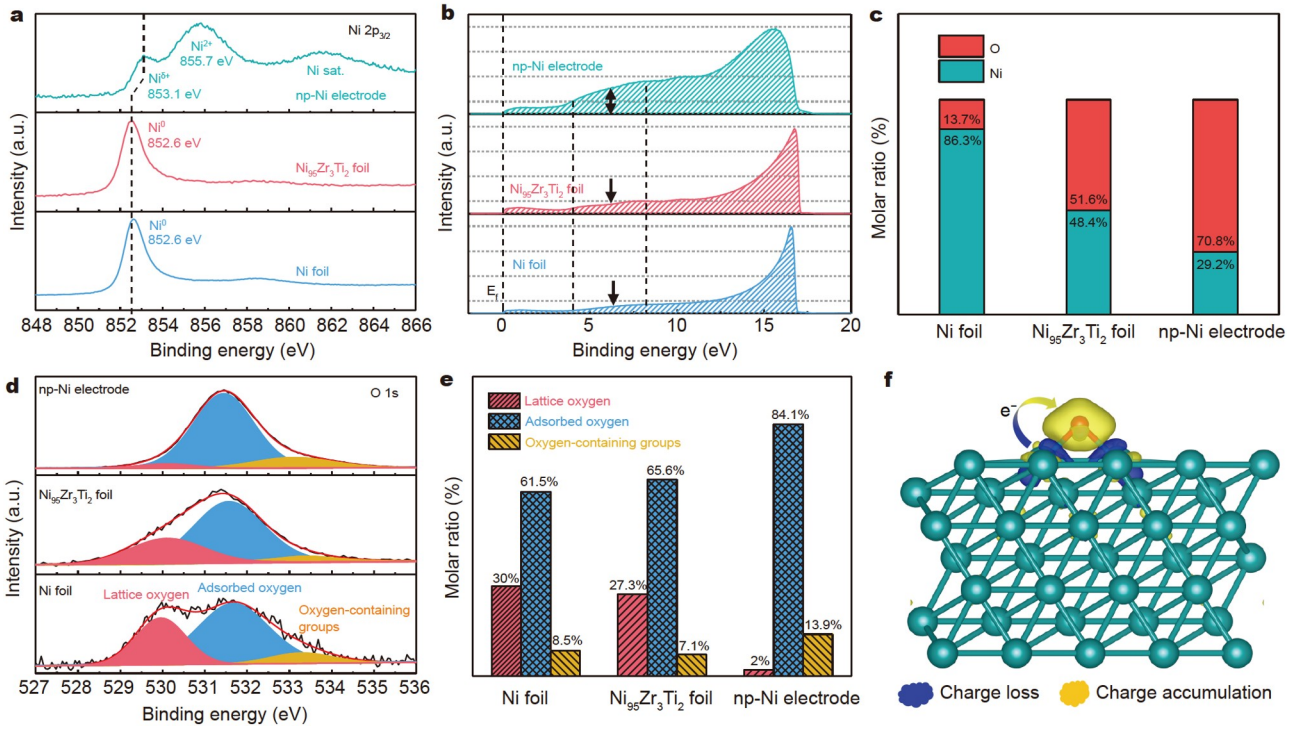

Figure 3 Surface chemical environment of the np-Ni electrode, $Ni_{95}Zr_3Ti_2$ foil, and Ni foil. (a) Ni $2p_{3/2}$ XPS spectra. (b) Peak intensity normalized UPS spectra. (c) Surface Ni/O molar ratio based on XPS results. (d) O 1s XPS spectra. (e) Statistical results of the molar ratio of various oxygen species based on (d). (f) Differential charge density of the Ni metal surface containing surface O termination. Red: O. Green: Ni.

model, has the best HER activity.

Generally, as the catalytic reaction mainly occurs on the surface of the catalyst, the role of these adsorbed oxygen species in alkaline HER should not be ignored. In this study, the DFT method was used to simulate the chemical structure of a water molecule near the O_{ads} on the Ni surface. As shown in Fig. 4a, when the catalyst/water molecular system is in the state of potential energy minimization, the interfacial water molecule is oriented with one of the electropositive H atoms pointing toward the O_{ads}, and the angle between three points ($\angle O_{ads}$-H1-O1) is 178.3°, similar to that in a hydrogen bond [41,42]. In this state, the distance between the O_{ads} and O1 is ~2.926 Å, and the lengths of the two H–OH bonds in the H_2O are 0.981 and 0.973 Å, respectively. Moreover, the bond angle of this water molecule is 104.7°, which is almost the same as that of ordinary water molecules (104.5°). No special effect between the O_{ads} and the H–OH bond is found, except for the orientation of the chemical bond.

Considering that the water molecules will shift in all directions under thermal motion, in reality, it is difficult to ensure that the distance between the H_2O molecule and the O_{ads} is always constant. As shown in Fig. 4b, when the distance between the O atom in H_2O and the O_{ads} is reduced to ~2.407 Å (under non-potential energy minimization), the angle ($\angle O_{ads}$-H1-O1, 179.2°) increases slightly than before, which is much closer to 180°. In particular, the bond lengths of the two H–OH bonds in this H_2O molecule change to 1.108 and 0.910 Å, respectively. The length of one H–OH bond is ~21.8% larger than that of another, and the included angle decreases to 98.8°. These results show that the O_{ads} can significantly change the chemical configuration of interfacial water molecules. More importantly, this leads to the formation of a catalyst/water molecular interface with hydrogen bond configuration—a process that is closely related to proton transfer [42–44]. In addition, the PDOS shown in Fig. 4c crosses the Fermi level, indicating the conductor characteristics of the O_{ads}, which are conducive to the electron transfer toward the H_2O through the O_{ads} site.

Based on the Ni-O_{ads} model, we propose a possible mechanism for the electrochemical dissociation of water molecules. As illustrated in Fig. 4d, the O_{ads} with a negative charge has electrostatic attraction and repulsion to the H and O atoms in the H_2O molecule, respectively. According to the Coulomb force formula ($F = KQ_1Q_2/r^2$), where K is a constant, Q_1 and Q_2 are the charge quantities of different point charges, respectively, and r is the distance between the point charges, in which the shorter the distance (r) is, the stronger the effect (F) is. To a certain extent, the electrostatic attraction of the O_{ads} to the H weakens the attraction of the O to the H in one H–OH bond, thus realizing the effect of activating water molecules. Driven by the potential energy from the external circuit, electrons transfer to protons through the O_{ads} site, and protons transfer to the O_{ads} site through the hydrogen bond, finally completing the dissociative adsorption of water molecules. Thus, it has been clearly demonstrated that the adsorbed oxygen atom is the key to realizing this mechanism.

CONCLUSIONS

In summary, integrated np-Ni electrodes were prepared by surface dealloying of $Ni_{45}Zr_{35}Ti_{20}$ MG ribbon, which exhibited extraordinary HER activity in an alkaline environment. Compared with bulk materials, np-Ni not only provides a larger surface area but also exhibits better intrinsic catalytic activity. Further studies showed that np-Ni can easily bond with oxygen and prefers to produce O_{ads}. In particular, the np-Ni catalysts,

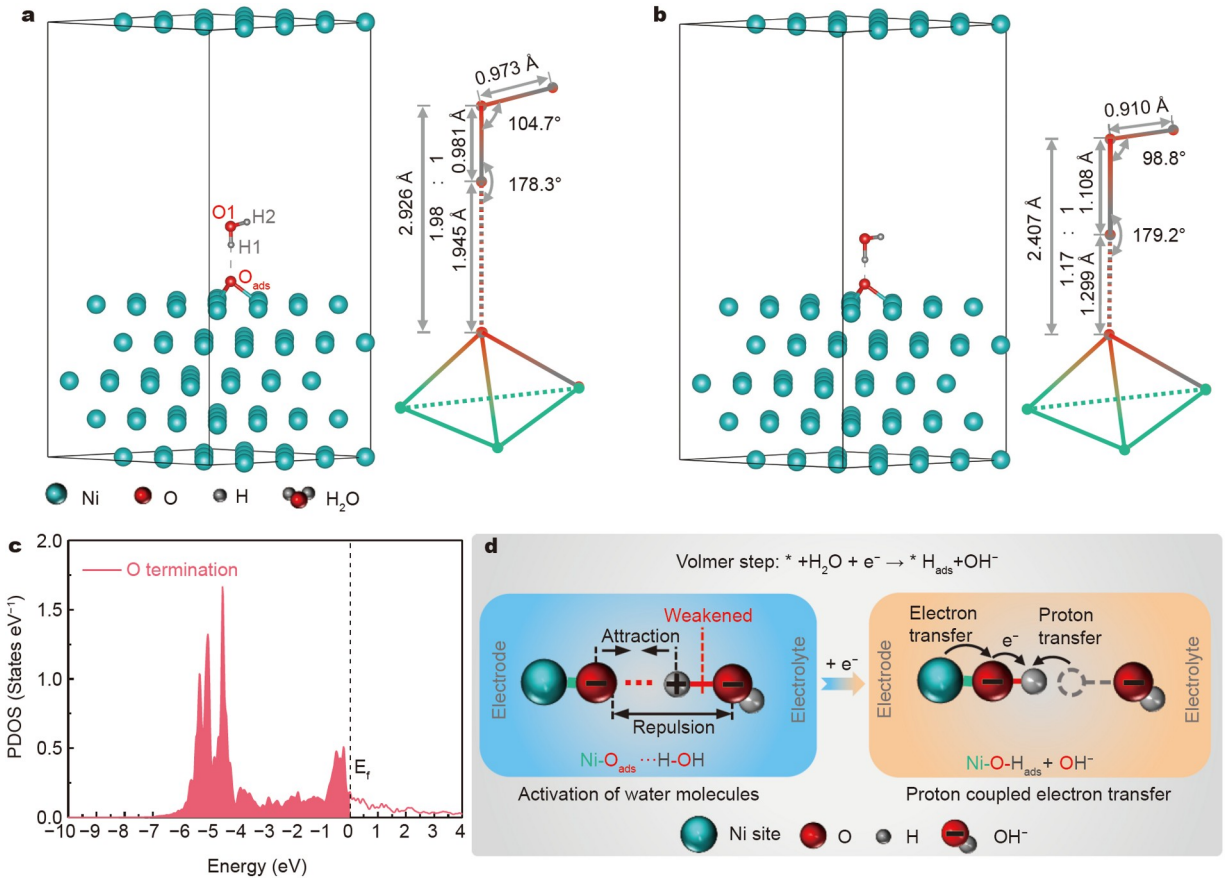

Figure 4 DFT calculation results based on the Ni-O_{ads} model and the proposed dissociation mechanism of water molecules. (a) Configuration and structural parameters of the Ni-O_{ads}/H_2O interface when the system is in the state of potential energy minimization. (b) Configuration and structural parameters of the Ni-O_{ads}/H_2O interface when one water molecule is closer to the O_{ads}. (c) PDOS plots of O 2p orbitals of surface O termination. (d) Schematic diagram of the proposed dissociation mechanism of water molecules. This highlights the electrostatic interaction between various atoms near the catalyst/water molecular interface.

whose surface structure characteristics better match the Ni-O_{ads} model, show the best HER activity. Moreover, DFT calculation results show that the Ni-O_{ads} surface can affect the chemical configuration of interfacial water molecules by constructing a hydrogen bonding structure. In turn, this is conducive to the cleavage of the H–OH bond. In addition, the conductor characteristics of the O_{ads} site are favorable for the proton-coupled electron transfer during the electrocatalytic process. Therefore, under the synergy of multiple favorable factors, the optimal np-Ni electrocatalyst can break through the limitation of sluggish water dissociation kinetics and realize efficient hydrogen production in an alkaline environment. This work not only identifies a high-performance electrocatalyst but also enriches the understanding of the dissociation mechanism of water molecules.

Received 2 December 2021; accepted 27 December 2021; published online 2 March 2022

1 Seh ZW, Kibsgaard J, Dickens CF, *et al.* Combining theory and experiment in electrocatalysis: Insights into materials design. Science, 2017, 355: eaad4998
2 Jiao Y, Zheng Y, Jaroniec M, *et al.* Jiao Y, Zheng Y. Design of electrocatalysts for oxygen- and hydrogen-involving energy conversion reactions. Chem Soc Rev, 2015, 44: 2060–2086
3 Debe MK. Electrocatalyst approaches and challenges for automotive fuel cells. Nature, 2012, 486: 43–51
4 Zheng Y, Jiao Y, Vasileff A, *et al.* The hydrogen evolution reaction in alkaline solution: From theory, single crystal models, to practical electrocatalysts. Angew Chem Int Ed, 2018, 57: 7568–7579
5 Marković NM, Schmidt TJ, Grgur BN, *et al.* Effect of temperature on surface processes at the Pt(111)-liquid interface: Hydrogen adsorption, oxide formation, and CO oxidation. J Phys Chem B, 1999, 103: 8568–8577
6 Schmidt TJ, Ross Jr. PN, Markovic NM. Temperature dependent surface electrochemistry on Pt single crystals in alkaline electrolytes. J Electroanal Chem, 2002, 524-525: 252–260
7 Ledezma-Yanez I, Wallace WDZ, Sebastián-Pascual P, *et al.* Interfacial water reorganization as a pH-dependent descriptor of the hydrogen evolution rate on platinum electrodes. Nat Energy, 2017, 2: 17031
8 Li L, Yu D, Li P, *et al.* Interfacial electronic coupling of ultrathin transition-metal hydroxide nanosheets with layered MXenes as a new prototype for platinum-like hydrogen evolution. Energy Environ Sci, 2021, 14: 6419–6427
9 Mahmood N, Yao Y, Zhang JW, *et al.* Electrocatalysts for hydrogen evolution in alkaline electrolytes: Mechanisms, challenges, and prospective solutions. Adv Sci, 2018, 5: 1700464
10 Li J, Zheng G. One-dimensional earth-abundant nanomaterials for water-splitting electrocatalysts. Adv Sci, 2017, 4: 1600380
11 Sheng W, Gasteiger HA, Shao-Horn Y. Hydrogen oxidation and evolution reaction kinetics on platinum: Acid *vs* alkaline electrolytes. J Electrochem Soc, 2010, 157: B1529
12 Rheinländer PJ, Herranz J, Durst J, *et al.* Kinetics of the hydrogen oxidation/evolution reaction on polycrystalline platinum in alkaline electrolyte reaction order with respect to hydrogen pressure. J Electrochem Soc, 2014, 161: F1448–F1457

13 Subbaraman R, Tripkovic D, Strmcnik D, *et al.* Enhancing hydrogen evolution activity in water splitting by tailoring Li^+-$Ni(OH)_2$-Pt interfaces. Science, 2011, 334: 1256–1260
14 Subbaraman R, Tripkovic D, Chang KC, *et al.* Trends in activity for the water electrolyser reactions on 3D M(Ni,Co,Fe,Mn) hydr(oxy)oxide catalysts. Nat Mater, 2012, 11: 550–557
15 Gong M, Zhou W, Tsai MC, *et al.* Nanoscale nickel oxide/nickel heterostructures for active hydrogen evolution electrocatalysis. Nat Commun, 2014, 5: 4695
16 Danilovic N, Subbaraman R, Strmcnik D, *et al.* Enhancing the alkaline hydrogen evolution reaction activity through the bifunctionality of $Ni(OH)_2$/metal catalysts. Angew Chem Int Ed, 2012, 51: 12495–12498
17 Pan Y, Zhang C, Lin Y, *et al.* Electrocatalyst engineering and structure-activity relationship in hydrogen evolution reaction: From nanostructures to single atoms. Sci China Mater, 2020, 63: 921–948
18 Daniel MC, Astruc D. Gold nanoparticles: Assembly, supramolecular chemistry, quantum-size-related properties, and applications toward biology, catalysis, and nanotechnology. Chem Rev, 2004, 104: 293–346
19 Liu L, Corma A. Metal catalysts for heterogeneous catalysis: From single atoms to nanoclusters and nanoparticles. Chem Rev, 2018, 118: 4981–5079
20 Peng S, Gong F, Li L, *et al.* Necklace-like multishelled hollow spinel oxides with oxygen vacancies for efficient water electrolysis. J Am Chem Soc, 2018, 140: 13644–13653
21 Wang H, Zhang X, Wang J, *et al.* Puffing quaternary $Fe_xCo_yNi_{1-x-y}P$ nanoarray *via* kinetically controlled alkaline etching for robust overall water splitting. Sci China Mater, 2020, 63: 1054–1064
22 Wang Z, Yang J, Wang W, *et al.* Hollow cobalt-nickel phosphide nanocages for efficient electrochemical overall water splitting. Sci China Mater, 2021, 64: 861–869
23 Zhang J, Chen Z, Liu C, *et al.* Hierarchical iridium-based multimetallic alloy with double-core-shell architecture for efficient overall water splitting. Sci China Mater, 2020, 63: 249–257
24 Deng L, Hu F, Ma M, *et al.* Electronic modulation caused by interfacial Ni-O-M (M=Ru, Ir, Pd) bonding for accelerating hydrogen evolution kinetics. Angew Chem Intl Edit, 2021, 60: 22276–22282
25 Ding Y, Chen M. Nanoporous metals for catalytic and optical applications. MRS Bull, 2009, 34: 569–576
26 Wittstock A, Zielasek V, Biener J, *et al.* Nanoporous gold catalysts for selective gas-phase oxidative coupling of methanol at low temperature. Science, 2010, 327: 319–322
27 Biener J, Biener MM, Madix RJ, *et al.* Nanoporous gold: Understanding the origin of the reactivity of a 21st century catalyst made by pre-columbian technology. ACS Catal, 2015, 5: 6263–6270
28 Liu P, Guan P, Hirata A, *et al.* Visualizing under-coordinated surface atoms on 3D nanoporous gold catalysts. Adv Mater, 2016, 28: 1753–1759
29 Chattot R, Le Bacq O, Beermann V, *et al.* Surface distortion as a unifying concept and descriptor in oxygen reduction reaction electrocatalysis. Nat Mater, 2018, 17: 827–833
30 Stukowski A, Markmann J, Weissmüller J, *et al.* Atomistic origin of microstrain broadening in diffraction data of nanocrystalline solids. Acta Mater, 2009, 57: 1648–1654
31 Belotti M, Lyu X, Xu L, *et al.* Experimental evidence of long-lived electric fields of ionic liquid bilayers. J Am Chem Soc, 2021, 143: 17431–17440
32 Volk S, Yazdani N, Yarema O, *et al. In situ* measurement and control of the Fermi level in colloidal nanocrystal thin films during their fabrication. J Phys Chem Lett, 2018, 9: 7165–7172
33 Zhong W, Chen L, Xiao S, *et al.* A versatile buffer layer for polymer solar cells: Rendering surface potential by regulating dipole. Adv Funct Mater, 2015, 25: 3164–3171
34 Conway BE, Tilak BV. Interfacial processes involving electrocatalytic evolution and oxidation of H_2, and the role of chemisorbed H. Electrochim Acta, 2002, 47: 3571–3594
35 Wang J, Xu F, Jin H, *et al.* Non-noble metal-based carbon composites in hydrogen evolution reaction: Fundamentals to applications. Adv Mater, 2017, 29: 1605838
36 Berlich A, Liu YC, Morgner H. Growth of nickel nanoparticles on NiO/Ni(001): Evidence of adsorbed oxygen on metal particles by metastable induced electron spectroscopy (MIES). Surf Sci, 2008, 602: 3737–3744
37 Rao CNR, Vijayakrishnan V, Kulkarni GU, *et al.* A comparative study of the interaction of oxygen with clusters and single-crystal surfaces of nickel. Appl Surf Sci, 1995, 84: 285–289
38 Kim CM, Jeong HS, Kim EH. NEXAFS and XPS characterization of molecular oxygen adsorbed on Ni(100) at 80 K. Surf Sci, 2000, 459: L457–L461
39 Hu Z, Qiu S, You Y, *et al.* Hydrothermal synthesis of $NiCeO_x$ nanosheets and its application to the total oxidation of propane. Appl Catal B-Environ, 2018, 225: 110–120
40 Wang M, Shen M, Jin X, *et al.* Oxygen vacancy generation and stabilization in CeO_{2-x} by Cu introduction with improved CO_2 photocatalytic reduction activity. ACS Catal, 2019, 9: 4573–4581
41 Desiraju GR. A bond by any other name. Angew Chem Int Ed, 2011, 50: 52–59
42 Arunan E, Desiraju GR, Klein RA, *et al.* Definition of the hydrogen bond. Pure Appl Chem, 2011, 83: 1637–1641
43 Geissler PL, Dellago C, Chandler D, *et al.* Autoionization in liquid water. Science, 2001, 291: 2121–2124
44 Vilčiauskas L, Tuckerman ME, Bester G, *et al.* The mechanism of proton conduction in phosphoric acid. Nat Chem, 2012, 4: 461–466

Acknowledgements This work was supported by the National Natural Science Foundation of China (51571151, 51701139, 51671143, 52177220, and 51804216).

Author contributions Hu Q and Chen Z designed and engineered the samples; Hu Q performed the experiments; Zheng X, Han X, and Hu W helped analyze the results; Hu Q wrote the paper with support from Deng Y. All authors contributed to the general discussion.

Conflict of interest The authors declare that they have no conflict of interest.

Supplementary information Experimental details and supporting data are all available in the online version of this paper.

Qingfeng Hu is a PhD student at the School of Materials Science and Engineering, Tianjin University. His recent research interests focus on the electrocatalytic hydrogen evolution behavior of transition metals and their derivatives with micro-nano structures in alkaline environments.

Zelin Chen received his PhD degree in material science from Tianjin University in 2020, under the supervision of Prof. Wenbin Hu and Prof. Yida Deng. At present, he works as a lecturer at the School of Materials Science and Engineering, Hainan University. His research interests include the design and controllable synthesis of noble-metal-based nanomaterials, the regulation of their surface and interface at the nanoscale, and their electrocatalytic applications in fuel cells.

Yida Deng was included in the "Changjiang Scholar Program" in 2021 and moved from Tianjin University to Hainan University as a chair professor. He received his PhD degree in materials science from Shanghai Jiao Tong University in 2006. Prof. Deng has extensive experience in the controllable synthesis of efficient electrocatalysts for energy storage and conversion, including noble and non-precious metallic nanomaterials, as well as their derivatives.

具有丰富吸附氧的纳米多孔镍用于高效碱性析氢电催化

胡庆丰[1], 陈泽霖[2*], 王嘉骏[1,3], 郑学荣[1], 韩晓鹏[1], 邓意达[1,2*], 胡文彬[1,3]

摘要 迟缓的水解离动力学严重限制了碱性电催化析氢反应的速率. 寻找高活性电催化剂, 并阐明水的解离机制具有挑战性和必要性. 本文通过对$Ni_{45}Zr_{35}Ti_{20}$金属玻璃前驱体进行表面脱合金处理, 制备了一体式纳米多孔镍(nanoporous nickel, np-Ni)电极. 在1 mol L^{-1} KOH溶液中, 该np-Ni电极在10 mA cm^{-2}电流密度下显示出20 mV的析氢过电位和快速的水解离动力学. 优异的性能不仅源于三维互连的导电网络提供的大表面积, 还源于其独特的表面性质带来的本征催化活性的增强. 进一步研究表明, 镍表面天然形成的氧组分类型对水分子的解离有重要影响. 特别是, 当晶格氧原子几乎消失时, 镍表面以吸附氧原子终止, 并表现出最快的水离解动力学. 密度泛函理论计算表明, 吸附氧原子作为镍金属的表面终止时, 附近的极性H_2O分子的取向和构型会受到吸附氧的强烈影响. 最终, 界面水分子的H–OH键可以以类似于氢键的方式被有效激活. 这项工作不仅提供了一种高性能/低成本的电催化剂, 而且深入研究了水解离的化学过程, 有利于电催化剂的合理设计.